Proceedings of the 5th International Conference on Materials Chemistry and Environmental Engineering
DOI: 10.54254/2755-2721/130/2025.20291

Injectable Hydrogel-Loaded Rough Heterostructured Nanoparticles for Multi-Procedural Promotion of Diabetic Wound Healing

Zhihan Hu[1,a,*,†], Jiayi Song[1,b,†], Mengdi Xie[1,c,†]

[1]*SDSZ International Department, Beijing, China*
a. grace.hu2008@outlook.com, b. jerrysong0523@outlook.com, c. oscartse@188.com
**corresponding author*
[†]*These authors contributed equally to this work and should be considered co-first authors.*

Abstract: Wound healing is a complex, multifaceted biological process broadly divided into four overlapping phases: hemostasis, inflammation, proliferation, and remodeling. Each stage of wound healing is critical to successfully restoring tissue integrity, and disruption or delay in any of these stages can lead to delayed healing. Various existing nanomaterials only promote a single stage. In this study, Au-CuS nanoparticles (Au-CuS NPs) with rough surfaces were formed by using gold nanorods (Au NRs) as templates on which copper sulfide (CuS) was grown and transported in an injectable hydrogel (Au-CuS@Gel). Au-CuS@Gel can accelerate all stages of diabetic wound healing. The rough surface of Au-CuS@Gel and the injectable property of hydrogel can adhere to close the wound and generate reactive oxygen species (ROS) under near infrared (NIR) light to effectively kill bacteria in diabetic wounds. Meanwhile, the rough morphology effectively polarizes macrophages to M2 phenotype and accelerates collagen deposition. Au-CuS@Gel can be programmed to promote all stages of diabetic wound healing. It provides a new paradigm for the healing of the special wounds represented by diabetes.

Keywords: Heydrogel, antibacterial, Au-CuS, wound healing.

1. Introduction

The incidence of chronic wounds is increasing with the global aging population and the rise in chronic diseases such as diabetes and cardiovascular disease, with approximately 2-3% of adults and older adults worldwide experiencing chronic wound problems [1]. Chronic wounds delay the healing process and may even progress to a permanent non-healing state, which is costly to treat and prone to a range of complications such as infection, pain, and dysfunction [2]. Diabetic foot ulcers are the most common chronic wounds with a large wound surface and poor prognosis, and the current state of treatment worldwide still faces many challenges [3]. Wound healing is a complex and delicate process involving multiple phases of hemostasis, inflammation, proliferation, and remodeling [4-6]. In the hemostatic phase, rapid formation of a closed layer at the wound site is necessary to prevent excessive loss of blood and body fluids; In the inflammatory phase, the presence of bacteria at the wound site can further exacerbate wound infection, so substances such as pathogenic bacteria need to be killed during the inflammatory phase; In the proliferation and remodeling phase, anti-

DOI: 10.54254/2755-2721/130/2025.20291

inflammatory factors (IL-10) secreted by M2 phenotype macrophages promote vascularization and collagen production [7, 8]. Wound healing requires the active cooperation of all phases to accelerate wound healing. Therefore, there is an urgent need to develop a drug that accelerates all phases of wound healing.

In recent years, the treatment of diabetic wounds has advanced with the development of nanotechnology [9]. Nanomaterials are now being used to create smart dressings with sensor capabilities to monitor wound conditions in real time and release medications as needed. Metal-based nanomaterials like Au [10] and Cu nanomaterials [11, 12], along with antimicrobial materials such as metal oxide ZnO [13], have proven effective in sterilizing wounds and reducing the risk of wound infection. Research has shown that rough nanomaterials play a role in promoting macrophage polarization, facilitating cell growth and regeneration, thereby enhancing the speed and quality of wound healing [14, 15]. Additionally, the rough structure has a better adhesion effect, which can close the wound trauma[16]. However, the clinical application and popularization of nanomaterial antimicrobial agents are currently subject to many limitations. For example, nanomaterials have a large band gap and can only be used to excite charge carriers with ultraviolet light, which makes patients prone to pain and burning [17]. In addition, nanomaterials have insufficient ability to generate reactive oxygen species (ROS) on their own, resulting in weak bacterial-killing ability. Near-infrared light (NIR) phototherapy is extensively used in various biomedical applications due to its advantages of strong tissue penetration and minimally invasive safety. Therefore, the development of nanomaterials that generate large amounts of ROS under NIR light is expected to be an alternative to antibiotics for wound treatment, thus facilitating all stages of wound healing.

Wound dressings are considered an effective method of delivering drugs directly to the wound surface. To date, a variety of wound dressings have been developed to promote wound healing, including porous foams [18], nanofibers, and functionalized hydrogels. Among the many dressings, hydrogel, as a hydrophilic polymer system with a three-dimensional (3D) cross-linked structure, retains large amounts of water and swells in aqueous media [19]. Due to their excellent biocompatibility and tunability, hydrogels are widely used in regenerative biomedical applications such as tissue engineering, drug delivery, and wound dressings [20]. Injectable hydrogels are used to form a stable gel structure when injected into the body and after injection. It has high fluidity and injectable type before injection, and after injection, the hydrogel is rapidly formed in the *in vivo* environment by temperature change, pH change, or enzymatic cross-linking reaction. Injectable hydrogels are controllable and stable and can be customized with appropriate hydrogel formulations and properties according to patient needs. Hyaluronic acid hydrogel is a hydrogel based on hyaluronic acid, which is widely found in human skin tissue and synovial fluid. However, while pure hyaluronic acid hydrogels are highly biodegradable, they lack a certain degree of flexibility. Silk fibroin, being a natural protein, can effectively overcome the brittleness of hyaluronic acid hydrogels. Furthermore, hyaluronic acid-silk fibroin hydrogels can combine the moisturizing and biocompatibility of hyaluronic acid and the biodegradability of sericin protein [21]. Therefore, the development of hyaluronic acid- Silk fibroin injectable hydrogels can be used to close large traumatic wounds for applied therapy.

In this study, the precious metal gold (Au) was used as a template to grow copper sulfide (CuS) on its surface to form surface rough morphostructured nanoparticles (Au-CuS NPs). Subsequently, the Au-CuS NPs were doped into silk fiber(SF)-doped hyaluronic acid (HA) injectable hydrogels (Figure 1a). The final formed Au-CuS@Gel was used to programmatically promote various processes of diabetic wound healing. In the hemostatic stage of wound healing, the injectable properties of hydrogels allow them to close irregular wounds in diabetic wounds, and their 3D structure absorbs exuding body fluids to achieve hemostasis. In the inflammatory stage of wound healing, the Au-CuS NPs transported by Au-CuS@Gel, as a typical plasma, have an enhanced localized plasmon

DOI: 10.54254/2755-2721/130/2025.20291

resonance effect (LSPR) to generate a large amount of reactive oxygen species (ROS) under the near-infrared light at 808 nm, and thus the Au-CuS@Gel can be used as an antimicrobial agent to kill the bacteria generated at the site of diabetic wounds, thus accelerating the antimicrobial wound healing process; meanwhile, the surface roughness morphology of Au-CuS NPs can induce macrophage polarization to an anti-inflammatory phenotype of M2, which in turn promotes cell proliferation and facilitates the proliferation and remodeling phases of wound healing (Figure 1b). This study provides a theoretical basis and reference for the treatment and repair of large traumatic wounds, such as diabetes mellitus, through the combination of injectable hydrogel and material modulation.

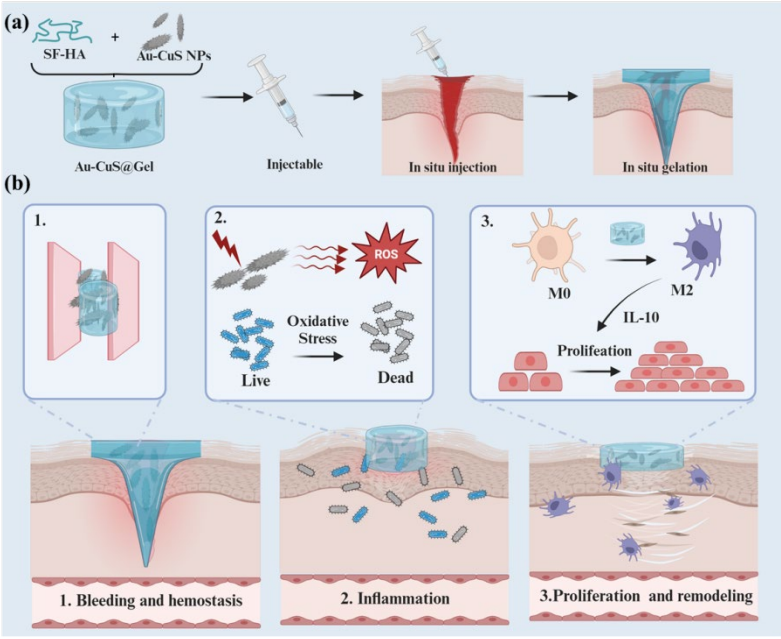

Figure 1: Schematic diagram of Au-CuS@Gel programmed to promote wound healing. (a) SF-AH hydrogel with Au-CuS NPs is an injectable hydrogel for in situ gelation at the wound site; (b1) In the hemostatic stage, Au-CuS@Gel has excellent adhesive properties that promote hemostasis; (b2) In the inflammation stage, ROS generated by Au-CuS NPs transported by Au-CuS@Gel under NIR light can be antimicrobial;(b3) In the proliferation and remodeling stage, Au-CuS NPs on the rough surface polarize macrophages to M2 phenotype and promote cell proliferation.

2. Materials and Methods

2.1. Materials

Hexadecyl trimethyl ammonium bromide (CTAB, 98%), chloroauric acid ($HAuCl_4 \cdot 3H_2O$), Hydroquinone (HQ), hydroquinone, copper (II) chloride ($CuCl_2$, 99%) and sodium sulfide ($Na_2S \cdot 9H_2O$, 99%) were purchased from Sigma-Aldrich. Sodium borohydride and potassium tetrachloroplatinate (K_2PtCl_4) were purchased from Adamas. Silver nitrate ($AgNO_3$) was purchased from Sinopharm. The water used to prepare the solutions during the experiment was deionized water.

2.2. Synthesis of Au nanorods (Au NRs)

The synthesis of Au NRs was achieved by the seed growth method [22]. To prepare for the seed solution, CTAB (5 mL, 0.1 M) solution was mixed with 5.0 mL of 0.1 M $HAuCl_4$. 0.6 mL of ice-cold 10 mM $NaBH_4$ was then added to the solution to deoxidize Au ions. After 30 min, excessive $NaBH_4$ solution was discharged. To prepare for the growth solution, CTAB (5 mL, 0.2 M) was mixed with 5

DOI: 10.54254/2755-2721/130/2025.20291

mL of 1 mM $HAuCl_4$. 120 μL of 0.1 M $AgNO_3$ was then added to the solution. Upon mixing with 600 μL of 0.1 M HQ as a strong reducing agent, the color of the solution changed from yellow to colorless. 320 μL of seed solution was added and left in darkness for 12 h. Subsequently, the mixture was centrifuged at a speed of 7000 rpm for 10 min.

2.3. Synthesis of Au-CuS NPs

10 mL of Au NRs was taken and mixed with 30 mL of deionized water. This solution was then centrifuged at a speed of 8000 rpm three times. 10 mL of 1 mM CTAB was added to the deposition, and the dissolution was accelerated using an ultrasonic cleaner. To the stirred solution, 400 μL of 1 mM K_2PtCl_4 was added. The solution was stirred for 5 min to make sure that $PtCl_4^{2-}$ had already been combined with gold particles. 1 mL of 100 mM $CuCl_2$ was added to this solution and stirred for 5 min. Subsequently, 8.6 mL of H_2O was added, and the solution was stirred for an additional 5 min. The solution was placed in the oven for 2 h. At this stage, the color of the solution changed from brownish-red to grey. Eventually, the metal nano nanoparticles were prepared by adding 500 μL of 1 mM $Na_2S·9H_2O$. The temperature of the solution was kept at 37 ℃. The final product was obtained by washing three times with H_2O.

2.4. Synthesis of SF-HA hydrogel and Au-CuS@Gel

MES solution (40 mL, 100 mM) was mixed with 1 g of HA. To the solution, 1.43 g of EDC and 0.86 g of NHS were added. The solution was stirred for 30 min. Subsequently, 0.86 g of TA was added to activate carboxyl groups. NaOH was gradually added until the solution reached a pH of 8. Following overnight stirring under the light-proof condition, the thoroughly mixed solution was transferred into a dialysis bag (Mw = 3.5 KDa), and the dialysis bag was immersed in sodium chloride (100 mM) solution for dialysis for 2 days, followed by an additional 2-day dialysis in deionized water. The contents within the dialysis bag were then freeze-dried. The resulting freeze-dried solid (HA-Tyr) was weighed, placed in a test tube, and mixed with silk fibroin (SF) to form SF-HA (where SF accounted for 25%). A quantitative amount of the prepared SF-HA was mixed with HRP (1 $U·mL^{-1}$) and H_2O_2 (1 mM) to generate a hydrogel with a concentration of 2% (w/v). Different concentrations of Au-CuS NPs were doped into SF-HA hydrogels (200, 100, 50, 25, and 12.5 μg/mL), which ultimately formed the hydrogel delivery system for transporting nanoparticles.

2.5. ROS performance

Total ROS production from Au-CuS@Gel was determined using 2,7-dichlorofluorescein diacetate (DCFH-DA). Assays were performed in 96-well plates by adding 80 μL DCFH-DA assay liquid and 20 μL Au-CuS@Gel material solution at different concentrations (200, 100, and 50 μg/mL) per well. The plates were irradiated with an 808 nm NIR laser at a power of 0.75 w/cm^2 for 7 min, incubated for 1 h at an excitation wavelength of 490 nm, and the fluorescence emission spectra were measured at 500 ~ 600 nm in a fluorescence spectrophotometer.

2.6. Antibacterial properties of Au-CuS@Gel under NIR light irradiation

Au-CuS@Gel was added to 1 mL of bacterial culture solution to prepare a 4 mg/mL solution. The grown bacterial solution was diluted until its absorption value at 600 nm was 0.1 and then was set aside. 100 μL of the prepared solution was extracted and combined with 900 μL of bacterial culture solution to formulate a solution of 400 μg/mL. The solution was further diluted pairwise to yield the concentration of 200 and 100 μg/mL. Afterwards, 50 μL of each concentration was dispensed into a 96-well plate, with each well replicated three times. Following this, 100 μL of bacterial solution

DOI: 10.54254/2755-2721/130/2025.20291

(absorption value = 0.1) was added to each well. The plate was then placed under NIR irradiation for 7 min before being transferred into the bacterial culture shaker (37 ℃, 150 rpm) for incubation. The absorption value at 600 nm was detected every 1 h to plot the growth curve. Meanwhile, antibacterial detection was performed by coating method as follows: 150 μL of bacterial solution was taken and mixed with 50 μL of Au-CuS@Gel (200 and 100 μg/mL). It was irradiated with NIR light (0.75 W/cm^2) for 7 min and then transferred to a bacterial culture shaker (37 ℃, 150 rpm) for 30 min. 1000-fold dilution of the above bacterial culture solution was performed, and 50 μL of this dilution was evenly spread on the solid medium, followed by an incubation period of 24 h. The photographs were taken for analysis.

2.7. Cell culture

Murine alveolar macrophages (RAW 264.7) and Human Umbilical Vein Endothelial Cells (HUVEC) were purchased from ATCC and cultured with Dulbecco's Modified Eagle Medium (DMEM) in a humidified 5% CO_2 atmosphere at 37 °C.

2.8. Cell viability assessment

4.8×10^4 RAW 264.7 cells were seeded into each well of a 96-well plate, while 6×10^3 HUVEC cells were placed in another 96-well plate. Both plates were incubated in a humidified 5% CO_2 incubator at 37°C for 24 h. The culture medium was then replaced with 100 μL of Au-CuS@Gel at different concentrations suspended in fresh culture medium. The cells were then further incubated for 6 h. For the NIR light group, Raw 264.7 cells and HUVEC cells containing Au-CuS@Gel were illuminated with 808 nm NIR light (0.75 W/cm^2, 7 min). In contrast, the control group, referred to as the dark group, was not treated. Subsequently, both groups were incubated for an additional 18 h. The top layer of the medium was removed and a heart-fresh medium containing 10% CCK-8 was added. The plates were then placed back into the humidified 5% CO_2 incubator at 37°C for another 4 h. The absorbance of CCK-8 at 450 nm was then measured to assess cell viability.

2.9. IL-10 and TNF-α anti-inflammatory cytokine quantification

4.8×10^4 Raw 264.7 cells were cultured overnight in 12-well plates. Then, the supernatant of Raw 264.7 cells was removed and 800 μL of fresh culture medium containing 100 μg/mL Au-CuS@Gel nanomaterial was added to each well. After 24 h of incubation, the supernatant of treated Raw 264.7 cells was collected and centrifuged at 1000 rpm for 4 min. The supernatant from each well was collected and the IL-10 and TNF-α levels were determined using the Mouse Interleukin-10 ELISA Kit (Elabscience) according to the instructions.

2.10. Cell proliferation assessment

Cell proliferation was assessed using a permeabilized well coculture system and the EdU-488 Cell Proliferation Kit (BeyoClickTM) containing Alexa Fluor 488. The procedure involved seeding 6×10^3 Raw 264.7 cells in each well of the upper chamber of the trans well, while 2.4×10^4 HUVEC cells were cultured in the lower chamber. After 24 h of incubation, the supernatant of the raw 264.7 cells was removed and 200 μL of fresh medium containing 100 μg/mL Au-CuS@Gel nanomaterials was added to the upper chamber. After 24 h, the proliferation rate of HUVEC cells in the lower chamber was detected using the Flour EdU-488 Cell Proliferation Assay Kit according to the instructions. The proliferation rate was then observed using laser scanning confocal microscopy.

DOI: 10.54254/2755-2721/130/2025.20291

3. Results and Discussion

3.1. Synthesis and characterization of Au NRs and Au-CuS NPs

Au NRs were first synthesized using the seed growth method. As shown in Figure 2 a,b, the final formed Au NRs have an aspect ratio of about 5:1, with a length of about 70 ± 9.67 nm and a width of about 11 ± 1.65 nm, and the Au NRs are relatively homogeneous and well dispersed. Furthermore, the Au NRs were used as templates to grow CuS on their surfaces.Pt^{2+} was first pre-attached to the surface of Au NRs using Pt^{2+} as an intermediate, then Cu^{2+} was added to replace the Pt^{2+} on the surface, and after the redox reaction, the Au-Cu_2O structure was formed first, and then the Au-CuS NPs were formed after the vulcanization of Na_2S. As illustrated in Figure 2b, c, the finally formed Au-CuS NPs remain well dispersed with a size of about 75 ± 5.68 nm. It is worth noting that the final formed Au-CuS NPs have obvious surface roughness with burr-like structure, which is due to the different deposition of CuS on the surface of Au NRs. The rough shell of CuS was found to be about 3.8 ± 0.9 nm by the magnified image of Figure 2d.

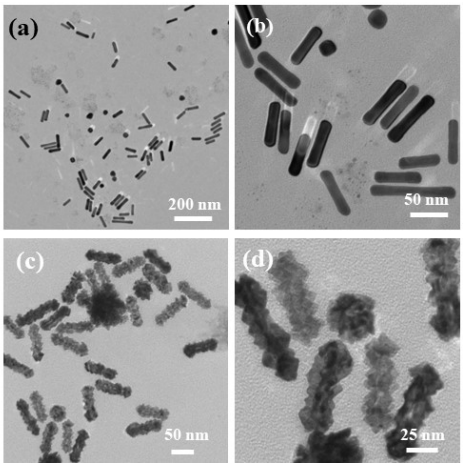

Figure 2: Morphological characterization. (a, b) TEM images of Au NRs; (b, c) TEM images of Au-CuS NPs.

3.2. Characterization of the properties of Au NRs and Au-CuS NPs

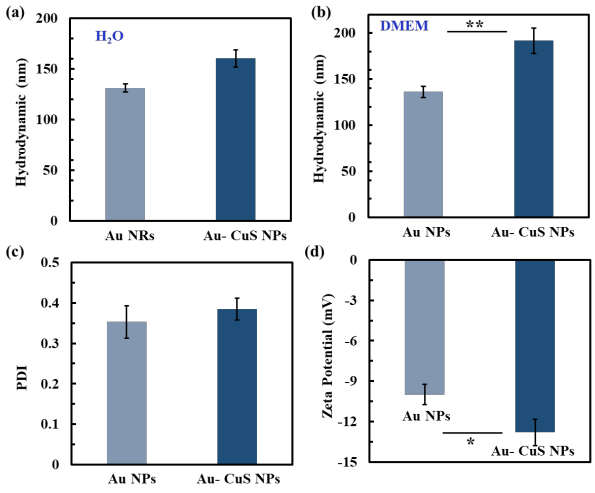

Figure 3: (a) Hydrated particle size maps of Au NRs and Au-CuS; (b) particle size maps of Au NRs and Au-CuS in DMEM; (c) value of PDI; and (d) zeta potential. *P<0.05, **P<0.01, ***P<0.001.

DOI: 10.54254/2755-2721/130/2025.20291

The particle size and potential of nanomaterials will affect the solubility, bioavailability, and targeting of nanoparticles. Therefore, dynamic light scattering (DLS) was used to further determine the particle size and potential of Au NRs and Au-CuS NPs. The results were as depicted in Figure 3a, the average hydrated particle size of Au NRs was 130.9 nm, and the hydrated particle size of Au-CuS NPs was about 160.43 nm. It can be found that the hydrated particle size of Au-CuS NPs is larger than that of Au NRs, which is due to the growth of CuS on the surface of Au NRs not only increases the size but also enhances its water solubility, resulting in a larger hydrated particle size. For better bioavailability, Au NRs and Au-CuS NPs were placed in DMEM cell culture medium, and the change value of their hydrated particle size was measured after 24 h of incubation. The results showed that the hydrated particle size of Au NRs in DMEM did not differ much from that in water, whereas the hydrated particle size of Au-CuS NPs in DMEM slightly increased compared to that in water (Figure 3b). This increase may be due to the change in the rough surface of Au-CuS NPs caused by the serum and other substances in DMEM. Furthermore, the PDI of both in water was tested, and the PDI values of Au NRs and Au-CuS NPs were about 0.36 (Figure 3c), which indicated that the two materials were well dispersed in the aqueous solution, and this result was consistent with that of Figure 3a. Finally, the zeta potentials of the two materials were tested and analyzed. The zeta potential of Au NRs was about -9.98, and that of Au-CuS NPs was about -12.78, which is because the growth of CuS on the surface of Au NRs further makes its potential negative (Figure 3d).

3.3. Optical properties of Au NRs and Au-CuS NPs

The optical absorption properties of the material are crucial for its subsequent biomedical applications. Therefore, a spectrophotometer (UV-Vis-NIR) was used to determine the absorbance of Au NRs and Au-CuS NPs in the range of 500-1000 nm. As demonstrated in Figure 4a, the absorption peak of Au NRs is located in the near-infrared region at 840 nm. The absorption curves of Au-CuS NPs were further examined, and the absorption of Au-CuS NPs did not change compared to that of Au NRs, which exhibits a strong absorption peak in the NIR region (Figure 4b). It is also found that the absorption peaks of Au-CuS NPs become broader compared to Au NPs, which is caused by the overlap of the absorption of the CuS shell with that of the central Au NRs. The near-infrared absorption of Au-CuS NPs provides the basis for the subsequent 808 nm illumination.

3.4. ROS generation measurement of Au-CuS NPs

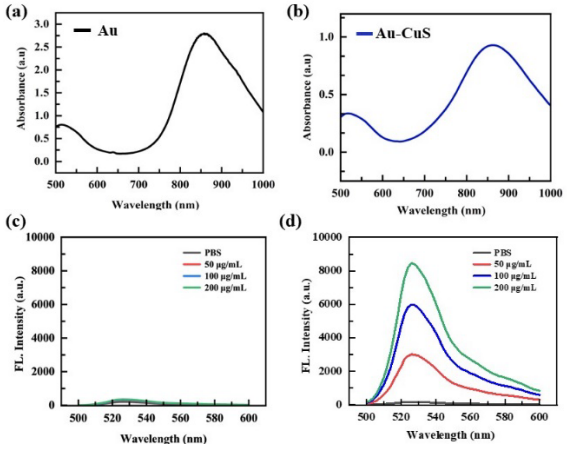

Figure 4: Performance determination of Au NRs and Au-CuS NPs. (a) Absorption images of Au NRs; (b) Absorption images of Au-CuS NPs; (c) Emission spectra of DCFH-DA of Au-CuS in PBS under dark conditions; (d) Emission spectra of DCFH-DA of Au-CuS in PBS under 808 nm laser irradiation (0.75 w/cm^2, 7 min).

DOI: 10.54254/2755-2721/130/2025.20291

From the above test results, the absorption of Au-CuS NPs is in the NIR region. When the incident light used matches the LSPR absorption peak of the material, the Au NPs undergo resonance energy transfer with CuS, and the Au-CuS produces photodynamic properties and generates a large amount of ROS. The ROS generation capacity of Au-CuS NPs was evaluated by DCFH-DA. In the dark state (no light), the fluorescence intensity of DCFH-DA was not different from that of the control group, indicating that Au-CuS NPs had no ROS production in the absence of light (Figure 4c). Next, the fluorescence intensity of DCFH-DA was detected by laser irradiation at 808 nm for 7 min (0.75 w/cm^2) on PBS solutions containing different concentrations of Au-CuS NPs. As known from the experimental results (Figure 4d), the fluorescence intensity of DCFH-DA of Au-CuS increased significantly after light irradiation. Meanwhile, the fluorescence intensity of DCFH-DA gradually increased with the concentration of Au-CuS NPs, which further indicated that the Au-CuS NPs had a strong ability to generate ROS, which laid the foundation for the subsequent use of ROS antibacterial.

3.5. Adhesion effects of Au-CuS@Gel

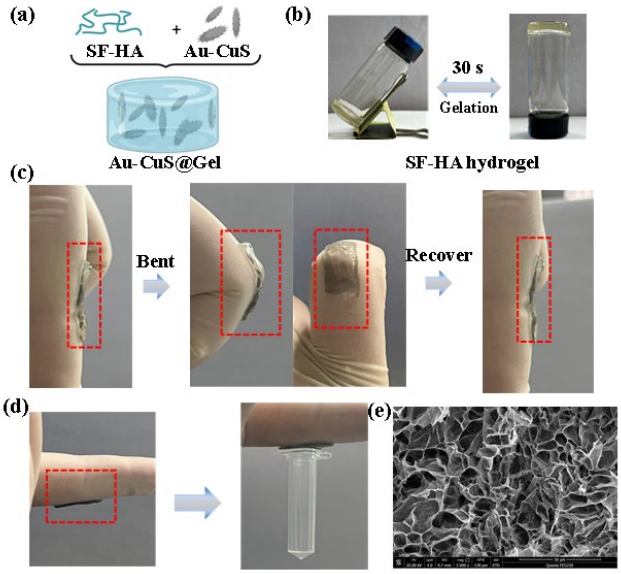

Figure 5: Performance testing of Au-CuS@Gel. (a) Schematic diagram of the composition of Au-CuS@Gel; (b) Vial inversion experiment with hydrogel formation; (c) Tensile property test of Au-CuS@Gel; (d) Adhesion property test of Au-CuS@Gel; (e) SEM image characterization of Au-CuS@Gel.

During the hemostatic phase of wound healing, the hydrogel fills the wound site, absorbs blood and body fluids exuded from the wound site, and adheres to the wound site to close the wound. Therefore, silk fiber-hyaluronic acid injectable hydrogel (SF-HA gel) was selected to promote the hemostatic process of wound healing with the help of Au-CuS NPs phase (Figure 5a). The gelation time of SF-HA was first determined by injecting the hydrogel into a vial, and the SF-HA gel was coagulated under HRP (1 U mL-1) and H_2O_2 (1 mM) conditions with a gelation time of 30 s (Figure 5b). The gelation time of 30 s allowed the injectable hydrogel to fill the wound site while preventing exudation into the surrounding tissue. The tensile properties of the Au-CuS@Gel were then further investigated. The Au-CuS@Gel was first injected into the mold to form the gel, which was then attached to the finger joints and stretched in multiple joint bends. As shown in Figure 5c, the hydrogel can be firmly adhered to the joint, and the hydrogel remains intact and does not break after the joint is bent, and after the joint is restored, the Au-CuS@Gel is still firmly adhered to the finger joint. The experiments

DOI: 10.54254/2755-2721/130/2025.20291

demonstrate that the Au-CuS@Gel exhibits good elastic flexibility. Subsequently, when the hydrogel adhered between the finger and the EP tube, the presence of Au-CuS@Gel allowed the EP tube to firmly adhere to the joint (Figure 5d) without detachment. The hydrogel has a porous 3D structure that mimics the structure of the skin, and this porous breathability facilitates wound repair. Therefore, the structure of Au-CuS@Gel was analyzed by scanning electron microscopy (SEM). The TEM results of Au-CuS@Gel are shown in Figure 5e, from which the final formed Au-CuS@Gel still maintains a macroporous structure, and this structure facilitates the application of Au-CuS@Gel to the wound site and maintains wound ventilation.

This experimental result indicates that Au-CuS@Gel not only possesses good tensile properties but also exhibits strong adhesive properties. These properties enable it to adhere effectively to the skin, close the wound at the wound site, and lay the foundation for the hemostatic process to promote wound healing.

3.6. Antimicrobial properties of Au-CuS@Gel

For the antibacterial experiments, we selected two colonies of *Escherichia coli* (a representative of Gram-negative bacteria) and *Staphylococcus aureus* (a representative of Gram-positive bacteria). The bacterial activity was examined by detecting the absorbance of the two bacteria at 600 nm after treatment with Au-CuS@NPs. Therefore, *Escherichia coli* (*E. coli*) and *Staphylococcus aureus* (*S. aureus*) were treated with Au-CuS@Gel to observe the effect of different concentrations of nanomaterials on bacterial activity at 808 nm NIR light condition (0.75 w/cm^2) and non-light condition. The experimental results showed that over time (Figure 6a, b), for both *E. coli* and *S. aureus*, the cellular activity of the two bacteria treated with the same concentration of Au-CuS@Gel without light was not significantly different from that of the control group treated with PBS, whereas the bacterial activity of the light group was much lower than that of the non-light group and the control group treated with PBS after being treated with 808 nm NIR light, indicating that Au-CuS@Gel has excellent antibacterial properties under NIR light. It can also be found that the bacterial activity is lower as the concentration of nanomaterials increases, indicating that Au-CuS@Gel inhibits bacterial growth more effectively. Among them, the group containing 200 μg/mL Au-CuS@Gel had the best antimicrobial performance against two types of bacteria under light conditions. It was followed by 100 μg/mL. Whereas Au-CuS@Gel did not have antibacterial properties for both bacteria under dark condition treatment. It should be noted that the trend of antibacterial performance of Au-CuS@Gel was consistent with the ROS-generating region of Figure 4 c, d, indicating that the excellent antibacterial performance of Au-CuS@Gel was due to the production of large amounts of ROS by Au-CuS NPs under NIR light.

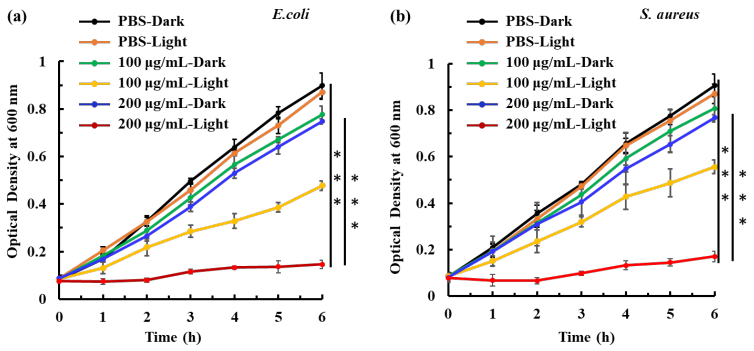

Figure 6: Antimicrobial properties of Au-CuS@Gel. (a) Growth curve of *E. coli* after Au-CuS@Gel treatment; (b) Growth curve of *S. aureus* after Au-CuS@Gel treatment. *P<0.05, **P<0.01, ***P<0.001.

DOI: 10.54254/2755-2721/130/2025.20291

To further visualize the antibacterial ability of Au-CuS@Gel, the colony-forming ability of two bacteria was observed using the agarose plate coating method. Au-CuS@Gel was incubated with bacteria and then subjected to both light and non-light treatments, followed by taking a certain number of bacteria for bacterial coating on the surface of the bacterial solid medium, and the colony formation was observed after 24 h. The experimental results in Figure 8a and b demonstrate a significant inhibition of *E. coli* and *S. aureus* colony formation following the treatment with Au-CuS@Gel and NIR laser irradiation. Particularly, the lowest bacterial colonies counts were observed at a 200 μg/mL concentration. In the dark state, the growth of both colonies was not inhibited. This experimental result is consistent with the above antimicrobial experimental results, indicating that Au-CuS@Gel has excellent antimicrobial properties under NIR light. At the same time, the excellent antimicrobial properties can effectively accelerate the inflammatory stage of wound healing.

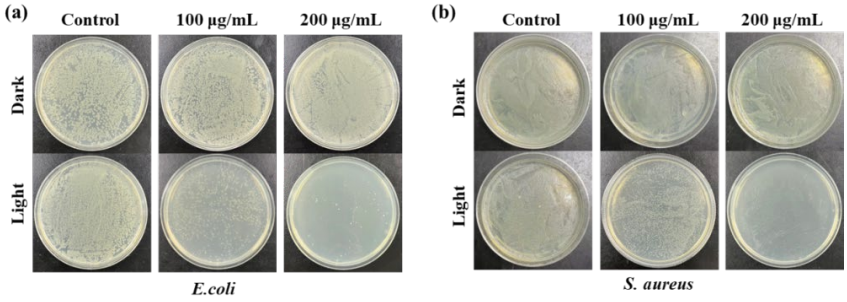

Figure 7: Bacterial Coating Experiment. (a) Plot of colony formation after Au-CuS@Gel treatment of *E. coli*; (b) Colony formation of Staphylococcus aureus after Au-CuS@Gel treatment.

3.7. Biosafety assessment

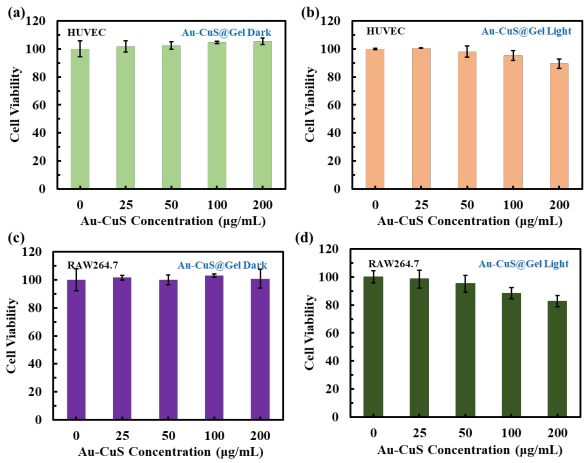

Figure 8: Biosafety analysis of Au-CuS@gel. Cellular activity of HUVEC cells treated with different concentrations of Au-CuS@Gel (0, 25, 50, 100, and 200 μg/mL) under (a) dark conditions and (b) 808 nm NIR light conditions; Cell activity of Raw264.7 cells treated with different concentrations of Au-CuS@Gel (0, 25, 50, 100 and 200 μg/mL) under (c) dark conditions and (d) 808 nm NIR illumination.

The biosafety assessment of wound dressings during the wound healing process is critical to the advancement of in vivo and clinical applications. Therefore, the biosafety of Au-CuS@gel was evaluated at the cellular level using HUVEC cells and RAW264.7 cells. The hydrogels were doped with different concentrations of Au-CuS NPs and co-cultured with the two cell line types, and the

DOI: 10.54254/2755-2721/130/2025.20291

survival rates of the cells under light versus dark conditions were examined using CCK-8. When the HUVEC cells and the RAW264.7 cells were treated in darkness (Figure 8a, c), the cell viability of the HUVEC cells without Au-CuS NPs was nearly 100%. As the concentration of Au-CuS NPs increased and more Au-CuS NPs were doped into the hydrogel, no significant cell death was found in HUVEC cells and RAW264.7 cells, indicating that Au-CuS@gel had good biocompatibility. Furthermore, the effect of Au-CuS@gel on cells was verified under near-infrared light conditions. When the HUVEC cells and the RAW 264.7 cells were treated with 0.75w/cm^2 NIR light at 808 nm (7 min) (Figure 8b, d), the cell viability of the HUVEC cells and RAW264.7 cells compared with those without Au-CuS NPs groups was also nearly 100%. With the increase of the concentration of Au-CuS NPs, it was also found that the cellular activity of RAW264.7 cells decreased by about 90% after treatment with Au-CuS@Gel containing 200 μg/mL. This reduction may be attributed to potential bio-damage caused by Au-CuS@gel under light exposure, although the material still maintains good biosafety. The improved biocompatibility of Au-CuS@Gel lays the foundation for subsequent therapeutic applications inside and outside the organism.

3.8. Macrophage polarization induced by Au-CuS@Gel

Normal macrophages have two phenotypes, including the M1 (pro-inflammatory) and M2 (anti-inflammatory) phenotypes. M2-polarized macrophages can positively influence wound healing. Studies have shown that nanomaterials with rough surface morphology can effectively promote macrophage polarization to the M2 phenotype. [14, 15] Therefore, the levels of tumor necrosis factor (TNF-α, a typical marker of M1 phenotype) and interleukin-10 (IL-10, a typical marker of M2 phenotype) were analyzed by ELISA. The results in Figure 9a show that, as a control, when RAW264.7 cells were exposed to complete darkness without Au-CuS nanomaterials, the levels of TNF-α and IL-10 were almost the same, both around 100 pg/mL. The amount of TNF-α produced by Au-CuS@Gel-treated cells was increased when exposed to 808 nm NIR light conditions, which was attributed to the fact that the ROS produced by Au-CuS@Gel under NIR light promoted partial polarization of macrophages, but the effect was small. The ability of Au-CuS@Gel to polarize Raw 264.7 to the M2 phenotype was further investigated. Compared with the control, the expression level of IL-10 in Raw 264.7 cells treated with Au-CuS@Gel at a concentration of 100 μg/mL averaged about 1900 pg/mL, which was much higher than that of the control as well as that of the TNF-α factor, both in light and non-light conditions (Figure 9b). This was since the morphological structure of Au-CuS NPs in Au-CuS@Gel stimulated macrophage polarization to the M2 phenotype.

The above experimental results suggest that Au-CuS@Gel can effectively polarize macrophages to the M2 phenotype after transporting Au-CuS NPs with rough surface structure, which has a positive effect on wound healing.

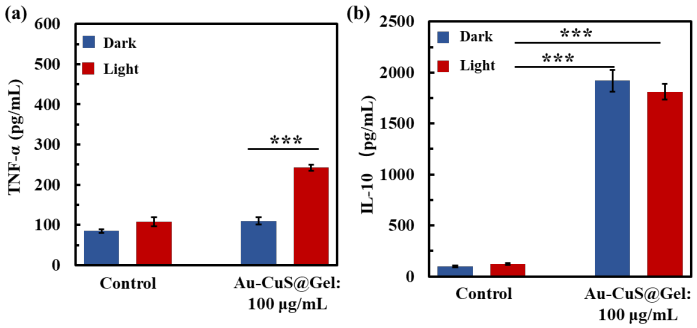

Figure 9: ELISA to assess the expression of various factors in Raw264.7 cells. (a) Expression of TNF-α in Raw264.7 cells after Au-CuS@Gel treatment; (b) Expression of IL-10 in Raw264.7 cells after Au-CuS@Gel treatment. *P<0.05, **P<0.01, ***P<0.001.

DOI: 10.54254/2755-2721/130/2025.20291

3.9. Cell proliferation induced by Au-CuS@Gel

When macrophages are polarized to the M2 phenotype, they promote cell proliferation and migration. Here, the transwell model was used to simulate the microenvironment of the wound site, and Raw 264.7 cells were inoculated in the upper chamber of the transwell, HUVEC cells were inoculated in the lower chamber, and Au-CuS NPs were added to the upper chamber, which induced the phenotypic polarization of Raw 264.7 cells and the secretion of anti-inflammatory factors, and the effect on HUVEC cells in the lower chamber was observed (Figure 10a). The proliferative capacity of HUVEC cells in the lower chamber was determined using the EDu-488 Cell Proliferation Kit. According to the experimental results in Figure 10b, it can be concluded that Au-CuS@Gel treated HUVEC cells showed more EDU-positive cells with stronger fluorescence intensity. It indicated that Au-CuS@Gel could effectively promote cell proliferation. This was attributed to the fact that the rough morphology of Au-CuS NPs in Au-CuS@Gel promoted the polarization of macrophages into M2 phenotype and the secretion of anti-inflammatory factors, which in turn promoted the proliferation of HUVEC cells. This experimental result also demonstrated that Au-CuS@Gel accelerated the proliferation and remodeling phases of wound healing.

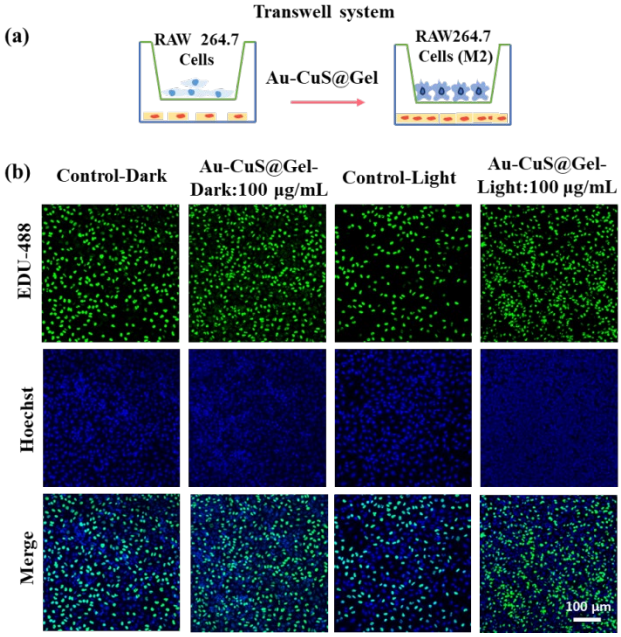

Figure 10: Cell proliferation assay. (a) Transwell system to simulate the microenvironment at the wound; (b) Study of the proliferative ability of Au-CuS@Gel on HUVEC cells.

4. Summary and Analysis

4.1. Summary

In this work, Au-CuS NPs with rough surface structures were synthesized and incorporated into SF-HA injectable hydrogels, and the resulting Au-CuS@Gel could be programmed to promote different stages of wound healing. In the hemostatic stage, Au-CuS@Gel has better elastic and adhesive properties and has the potential to close irregular wounds such as diabetic wounds. In the inflammatory stage, the production of large amounts of ROS by Au-CuS@Gel under near-infrared light can effectively inhibit the growth of *E. coli* and *S.aureus* as well as the formation of colonies, which would be beneficial to promote the process of the inflammatory stage of wound healing. In the proliferation and remodeling phase, Au-CuS@Gel can polarize macrophages to the M2 phenotype

DOI: 10.54254/2755-2721/130/2025.20291

and thus promote the proliferation of HUVEC cells, which is conducive to wound healing. This study integrates wound healing therapy and fills the gap of the uniqueness of nanomaterials for the treatment of chronic wounds such as diabetes, providing a strong rationale for accelerating the wound healing process.

4.2. Limitations analysis

There are still some limitations despite the promising clinical application of Au-CuS@Gel in the treatment of diabetic-like large traumatic wounds.

Lack of experimental data: the adhesion and tensile properties against Au-CuS@Gel were not tested using mouse skin. Meanwhile, the current treatment achieved good therapeutic results at the cellular level and lacked in vivo and clinical validation.

Antibacterial mechanism of ROS: The ROS generated by Au-CuS@Gel has excellent antimicrobial properties, but the antimicrobial mechanism of ROS for bacteria still needs to be further investigated.

Long-term safety: the hydrogel acts as a carrier and the encapsulated Au-CuS NPs may be released at the skin wound, so the long-term safety of Au-CuS@Gel in vivo still needs to be considered.

4.3. Future Prospects

Nanomaterials combined with hydrogels to form nanohydrogels are used to programmatically promote various stages of wound healing, representing a promising therapeutic approach with significant potential for future clinical applications.

Multi-scenario application: Au-CuS@Gel works at all stages of wound healing to promote the healing process, so it can be applied to multiple types of wounds at any stage. This has significant implications for its clinical application and future development.

Personalization: Hydrogel, as a typical wound dressing, can transport not only nanomaterials but also multiple types of therapeutic drugs. It can be customized for precise treatment according to the patient's clinical presentation.

High therapeutic effect and short treatment time: the system integrates nanomaterials with hydrogels, with nanomaterials enhancing the adhesive properties of the hydrogel while the hydrogel fills the void of nanomaterials to treat a single scene, the two synergize with each other, the treatment will be integrated, and at the same time, SF-HA has excellent biocompatibility, the system to effectively improve the therapeutic effect of wound healing.

Overall, the Au-CuS@Gel system in this study was multi-step programmed to promote all stages of wound healing and accelerate wound healing. This system holds promise for the clinical management of large chronic wounds typical of diabetic patients. Future studies will further investigate its advantages and clinical application in the treatment of chronic wounds, which will be an important reference for improving the prognosis of patients.

References

[1] *L. M. Morton and T. J. Phillips. Wound healing and treating wounds Differential diagnosis and evaluation of chronic wounds. Journal of the American Academy of Dermatology 2016, 74, 4, 589-605.*

[2] *A.-L. Pignet, M. Schellnegger, A. Hecker, L.-P. Kamolz and P. Kotzbeck. Modeling Wound Chronicity In Vivo: The Translational Challenge to Capture the Complexity of Chronic Wounds. Journal of Investigative Dermatology 2024, 144, 7, 1454-1470.*

[3] *T. Zgonis, J. J. Stapleton, V. A. Girard-Powell and R. T. Hagino. Surgical management of diabetic foot infections and amputations. AORN journal 2008, 87, 5, 935-946; quiz 947-950.*

[4] *M. Parani, G. Lokhande, A. Singh and A. K. Gaharwar. Engineered Nanomaterials for Infection Control and Healing Acute and Chronic Wounds. Acs Applied Materials & Interfaces 2016, 8, 16, 10049-10069.*

DOI: 10.54254/2755-2721/130/2025.20291

[5] M. C. Linju and M. R. Rekha. Role of inorganic ions in wound healing: an insight into the various approaches for localized delivery. Therapeutic delivery 2023, 14, 10, 649-667.
[6] H. Yu, Y. Wang, D. Wang, Y. Yi, Z. Liu, M. Wu, Y. Wu and Q. Zhang. Landscape of the epigenetic regulation in wound healing. Frontiers in Physiology 2022, 13, 949498.
[7] C. J. Ferrante and S. J. Leibovich. Regulation of Macrophage Polarization and Wound Healing. Advances in wound care 2012, 1, 1, 10-16.
[8] R. Sridharan, A. R. Cameron, D. J. Kelly, C. J. Kearney and F. J. O'Brien. Biomaterial based modulation of macrophage polarization: a review and suggested design principles. Materials Today 2015, 18, 6, 313-325.
[9] P. Yudaev, Y. Mezhuev and E. Chistyakov. Nanoparticle-Containing Wound Dressing: Antimicrobial and Healing Effects. Gels 2022, 8, 6, 329.
[10] J. Toczek, M. Sadlocha, K. Major and R. Stojko. Benefit of Silver and Gold Nanoparticles in Wound Healing Process after Endometrial Cancer Protocol. Biomedicines 2022, 10, 3, 679.
[11] J.-G. Leu, S.-A. Chen, H.-M. Chen, W.-M. Wu, C.-F. Hung, Y.-D. Yao, C.-S. Tu and Y.-J. Liang. The effects of gold nanoparticles in wound healing with antioxidant epigallocatechin gallate and α-lipoic acid. Nanomedicine-Nanotechnology Biology and Medicine 2012, 8, 5, 767-775.
[12] W. Diao, P. Li, X. Jiang, J. Zhou and S. Yang. Progress in copper-based materials for wound healing. Wound Repair and Regeneration 2024, 32, 3, 314-322.
[13] B. Vu Khac Hoang, D. Park and Y.-C. Lee. Chitosan Combined with ZnO, TiO₂ and Ag Nanoparticles for Antimicrobial Wound Healing Applications: A Mini Review of the Research Trends. Polymers 2017, 9, 1, 21.
[14] T. U. Luu, S. C. Gott, B. W. K. Woo, M. P. Rao and W. F. Liu. Micro- and Nanopatterned Topographical Cues for Regulating Macrophage Cell Shape and Phenotype. Acs Applied Materials & Interfaces 2015, 7, 51, 28665-28672.
[15] J. Li, J. Wen, B. Li, W. Li, W. Qiao, J. Shen, W. Jin, X. Jiang, K. W. K. Yeung and P. K. Chu. Valence State Manipulation of Cerium Oxide Nanoparticles on a Titanium Surface for Modulating Cell Fate and Bone Formation. Advanced Science 2018, 5, 2, 1700678.
[16] A. Meddahi-Pelle, A. Legrand, A. Marcellan, L. Louedec, D. Letourneur and L. Leibler. Organ repair, hemostasis, and in vivo bonding of medical devices by aqueous solutions of nanoparticles. Angewandte Chemie (International ed. in English) 2014, 53, 25, 6369-6373.
[17] C. Wei, W. Y. Lin, Z. Zainal, N. E. Williams, K. Zhu, A. P. Kruzic, R. L. Smith and K. Rajeshwar. Bactericidal activity of TiO2 photocatalyst in aqueous-media - toward a solar-assisted water disinfection system. Environmental Science & Technology 1994, 28, 5, 934-938.
[18] E.-H. Song, S.-H. Jeong, J.-U. Park, S. Kim, H.-E. Kim and J. Song. Polyurethane-silica hybrid foams from a one-step foaming reaction, coupled with a sol-gel process, for enhanced wound healing. Materials Science and Engineering C-Materials for Biological Applications 2017, 79, 866-874.
[19] I. I. Preobrazhenskii and V. I. Putlyaev. 3D Printing of Hydrogel-Based Biocompatible Materials. Russian Journal of Applied Chemistry 2022, 95, 6, 775-788.
[20] S. Jacob, A. B. Nair, J. Shah, N. Sreeharsha, S. Gupta and P. Shinu. Emerging Role of Hydrogels in Drug Delivery Systems, Tissue Engineering and Wound Management. Pharmaceutics 2021, 13, 3, 357.
[21] S. Ilic-Stojanovic, L. Nikolic and S. Cakic. A Review of Patents and Innovative Biopolymer-Based Hydrogels. Gels 2023, 9, 7, 556.
[22] J. Liu, J. N. Duggan, J. Morgan and C. B. Roberts. Seed-mediated growth and manipulation of Au nanorods via size-controlled synthesis of Au seeds. Journal of Nanoparticle Research 2012, 14, 12, 1289.